Surface structure of $\sqrt{3}\times\sqrt{3}R\,30°$ Cl/Ni(111) determined using low-temperature angle-resolved photoemission extended fine structure

Li-Qiong Wang, Z. Hussain, Z. Q. Huang, A. E. Schach von Wittenau, D. W. Lindle,* and D. A. Shirley
Department of Chemistry, University of California, Berkeley, California 94720
and Materials and Chemical Sciences Division, Lawrence Berkeley Laboratory, 1 Cyclotron Road, Berkeley, California 94720
(Received 23 April 1991)

A surface structural study of the $\sqrt{3}\times\sqrt{3}R\,30°$ Cl/Ni(111) adsorbate system was made using low-temperature angle-resolved photoemission extended fine structure. The experiments were performed along two emission directions, [111] and [110], and at two temperatures, 120 and 300 K. The multiple-scattering spherical-wave analysis determined that the Cl atom adsorbs in the fcc threefold hollow site, 1.837(8) Å above the first nickel layer, with a Cl—Ni bond length of 2.332(6) Å, and an approximate 5% contraction between the first and the second nickel layers (the errors in parentheses are statistical standard deviations only).

I. INTRODUCTION

Adsorbed atoms or molecules frequently cause relaxations of substrate surfaces. However, the understanding of adsorbate-induced substrate surface relaxation requires accurate and detailed surface and near-surface structural information. Angle-resolved photoemission extended fine structure (ARPEFS) (Refs. 1–5) has proven to be a powerful tool in this regard.

ARPEFS is the angle-resolved and energy-dependent form of photoelectron diffraction due to the final-state interference between the direct and the scattered photoelectron waves.[6] Fourier transformation of the extended fine structure provides direct and qualitative structural information. However, the more quantitative structural analysis requires multiple-scattering spherical-wave (MSSW) theory.[7] With a MSSW level analysis, effects as subtle as small corrugation and relaxation near the substrate surface can be characterized. Because thermal effects (larger mean-square-relative atomic displacements) reduce the amount of structural information present in the fine structure, cooling the lattice effectively extends the range of ARPEFS to deeper layers. Recent studies[5,8] have shown that the adsorbate geometry and the substrate relaxation can be determined more accurately by using low-temperature ARPEFS. In this paper, we employ low-temperature ARPEFS to study the $\sqrt{3}\times\sqrt{3}R\,30°$ Cl/Ni(111) system.

There are several published reports of structural studies of halogen atoms on metal surfaces. For example, the $c(2\times2)$ Cl/Cu(001) system has been studied by several groups.[5,9–11] However, there are few studies of halogen atoms on fcc (111) surfaces. In a surface-extended x-ray-absorption fine structure (SEXAFS) study of $\sqrt{3}\times\sqrt{3}R\,30°$ Cl/Cu(111), Woodruff *et al.*[12] were unable to obtain accurate distances beyond the first-nearest neighbors, or to distinguish the two different threefold hollow adsorption sites of the fcc (111) surface. However, these two inequivalent hollow sites were distinguished in their photoelectron diffraction study, where only the distance from Cl to the first substrate layer was given. Since ARPEFS has high directional sensitivity, the different substrate atoms can be emphasized by choosing different emission geometries. Thus, ARPEFS can clearly distinguish between two kinds of threefold adsorption sites. In our study, we use low-temperature ARPEFS to determine the adsorption site as well as to obtain an accurate distance to the second substrate layer for the $\sqrt{3}\times\sqrt{3}R\,30°$ Cl/Ni(111) system. Interestingly, Kuroda *et al.*[13] recently reported a study of the same Cl/Ni(111) system using a combination of SEXAFS and the x-ray standing-wave method. They found no substrate surface relaxations in the $\sqrt{3}\times\sqrt{3}R\,30°$ Cl/Ni(111), as opposed to the $p(2\times2)$ S/Ni(111) (Ref. 14), where a significant contraction of 15% was observed with respect to the bulk spacing. Thus, their study offers an opportunity to compare the structural results obtained from different techniques.

This paper is organized as follows. Section II gives the experimental details and the procedures of data collection and reduction. Section III describes two types of analysis: Fourier and multiple-scattering analysis, and present results. Section IV discusses and compares the results. A summary and conclusions are given in Sec. V.

II. EXPERIMENT

The experiments were performed on Beamline X24A (Ref. 15) at the National Synchrotron Light Source at Brookhaven using a Ge(111) double-crystal monochromator. The Cl 1*s* photoemission spectra were taken in the kinetic-energy range from 50 to 550 eV, with photon

energies from 2870 to 3370 eV. The resolution of the double-crystal monochromator was approximately 1 eV through this photon energy range. Data were collected with a rotatable hemispherical electrostatic analyzer[16] which has the energy resolution of ~ 1 eV full width at half maximum (FWHM) under the operating conditions of 160-eV pass energy, and the angular resolution of the input lens of $\pm 3°$. The experimental chamber was equipped with a four-grid combined low-energy-electron-diffraction (LEED) and Auger system, an ion gun, and an effusive beam doser for introducing chlorine gas.

A nickel single crystal was cut, oriented to within $\pm 1°$ of the (111) direction as determined by Laue backscattering, then mechanically polished and chemically etched. Since the fcc (111) crystal lacks twofold symmetry, it is hard to tell the crystal azimuthal orientation from the $p(1\times 1)$ LEED pattern. Thus, several Laue pictures were taken at different x-ray incident directions along the fixed crystal axis to define the azimuthal orientation of the crystal. The final finished crystal was attached to a Ta sample plate mounted on a high-precision manipulator with a liquid-nitrogen cooling system. Sample heating was accomplished by electron bombardment from a tungsten filament located behind the sample plate. The temperatures were measured by a chromel-alumel thermocouple attached to the sample plate next to the sample. The nickel crystal was cleaned by repeated cycles of Ar^+-ion sputtering and annealing to about 880 K. This procedure was sufficient to remove all impurities except carbon. Carbon was then removed by heating the crystal to 770 K after exposure to 1×10^{-8} Torr of oxygen for several minutes. The crystal was taken as clean when Auger electron spectroscopy (AES) showed no detectable traces of carbon, nitrogen, oxygen, or sulfur contamination and a sharp $p(1\times 1)$ LEED pattern was observed. The chamber pressure was about 3×10^{-10} Torr during measurements. Because chlorine exposure to a clean Ni(111) surface produces a sequence of LEED patterns with superstructures, and a sharp $\sqrt{3}\times\sqrt{3}R\,30°$ LEED pattern is stable within a relatively small exposure range corresponding to ~ 0.2 L, the $\sqrt{3}\times\sqrt{3}R\,30°$ Cl overlayer preparation was done carefully in several steps. A sharp $\sqrt{3}\times\sqrt{3}R\,30°$ Cl overlayer LEED pattern was produced by dosing Cl_2 through an effusive beam doser at room temperature for a total of 4–5 min with the main chamber pressure at $\sim 1\times 10^{-9}$ Torr. This was followed by 350-K annealing for 2 min to dissociate Cl_2 completely into atomic Cl.

The experiments were carried out along two emission directions, [111] and [110], and at two temperatures, 120 ± 5 K and 300 K. These four set of ARPEFS data were taken on separately prepared samples. The sample was flashed to about 350 K every 6–9 h during data collection, and more often for the low-temperature measurements. The crystal orientation angle for each geometry was determined by a He-Ne laser autocollimation through the experimental chamber viewports with an accuracy of $\pm 2°$. The experimental geometries are shown in Fig. 1. For the normal [111] geometry, photoelectrons were collected along the surface normal with the photon

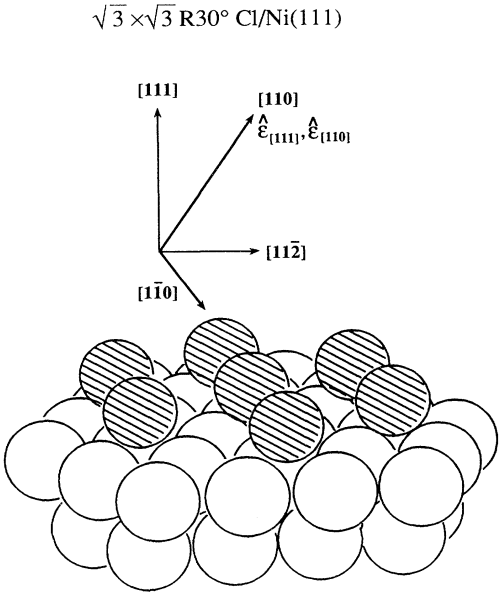

FIG. 1. A view of the $\sqrt{3}\times\sqrt{3}R\,30°$ overlayer of chlorine (shaded atoms) on the (111) face of a nickel single crystal. The emission directions are labeled [111] and [110], while the photon polarization vectors associated with each geometry are labeled $\hat{\varepsilon}_{[111]}$ and $\hat{\varepsilon}_{[110]}$, respectively.

polarization vector 35° from the surface normal toward the [11$\bar{2}$] direction, while for the off-normal [110] geometry, the emission direction and photon polarization vector are collinear along the [110] direction. These two geometries were chosen to highlight nearby backscattering atoms, utilizing the directional sensitivity of ARPEFS. The [111] geometry can determine interlayer spacings effectively, while the [110] geometry was selected to emphasize the nearest neighbors along the [110] direction.

For each emission geometry at a given temperature, a series of photoemission spectra was collected over a 50–550-eV kinetic-energy range in equal electron wavenumber increments of 0.08 Å^{-1}. Each photoemission spectrum was centered on the Cl 1*s* photoelectron peak, with an energy window 25–30 eV. The experimental background consisted of three photoemission scans covering the kinetic-energy range of 40–560 eV. Each scan was taken at a different photon energy so that the Cl 1*s* photoemission peak lay about 10 eV below the lowest kinetic energy in each spectrum. This experimentally measured background was used in the least-squares fitting for the normalization of each photoemission spectrum to compensate for the inhomogeneous photon flux and the electron analyzer transmission function. The photoemission intensity was extracted by least-squares fitting of each photoemission spectrum with three functions: a Voigt function to model the core-level photoelectron peak, a Gaussian convoluted with a step function (*G* step) to describe the inelastically scattered electrons associated

with the photoelectron peak, and an experimentally measured background to account for other inelastic-scattering processes. The detailed procedures have been described previously.[5]

In analogy to EXAFS, the total normalized photoemission intensity $I(E)$ as a function of kinetic energy E is composed of a slowly varying atomiclike portion and a rapidly oscillating contribution due to the interference effects of electron scattering from neighboring ion cores. $I(E)$ can be described as

$$I(E)=[\chi(E)+1]I_0(E) , \tag{1}$$

where $I_0(E)$ is a slowly varying atomiclike function and $\chi(E)$ is the oscillatory interference function, which can be determined by removing the slowly varying function $I_0(E)$ from the total photoemission intensity $I(E)$:

$$\chi(E)=\frac{I(E)-I_0(E)}{I_0(E)} . \tag{2}$$

The experimental $\chi(E)$ curves are shown in Fig. 2 for the [111] and [110] data at two temperatures, 120 and 300 K, respectively. $I_0(E)$ was fitted with simple low-order polynomials for constructing $\chi(E)$ curves. We can see from Fig. 2 that the oscillation amplitudes of $\chi(E)$ at the lower temperature are enhanced as compared with those at room temperature. The oscillation patterns are matched well at the two temperatures.

For Fourier data analysis, it is necessary to convert $\chi(E)$ to $\chi(k)$. The photoelectron kinetic energy E measured outside the solid is related to the wave number k of the photoelectron inside the solid by the de Broglie relation

$$k=\hbar^{-1}\sqrt{2m_e(E+V_0)} , \tag{3}$$

where m_e is the electron rest mass and V_0 the inner potential of the solid. The value of V_0 is typically about 10 eV, but the exact value is unknown. The V_0 is therefore treated as an adjustable parameter in the fits.

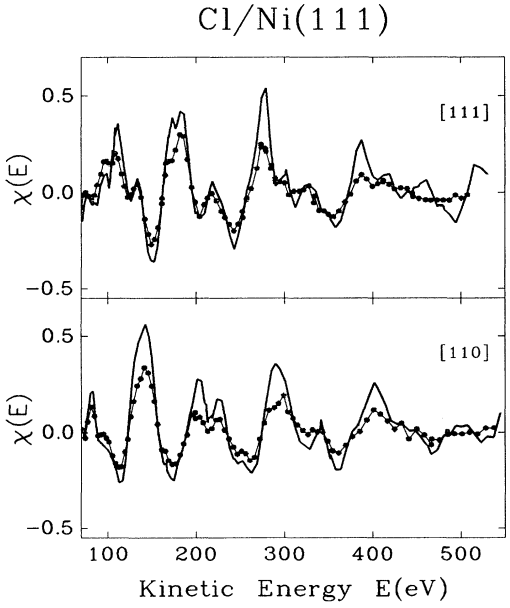

FIG. 2. Experimental $\chi(k)$ curves for the [111] and the [110] geometries. The curve with solid dots is $\chi(k)$ at 300 K, and the heavier curve is $\chi(k)$ at 120 K.

III. ANALYSIS AND RESULTS

Structural information can be extracted from the experimental $\chi(k)$ curves in two ways: by Fourier analysis and by multiple-scattering spherical-wave (MSSW) analysis. We first treat the data by Fourier analysis to obtain qualitative structural information such as adsorption site and approximate geometric parameters. MSSW calculations are then required to obtain quantitative structural information.

A. Fourier analysis

Using the single-scattering model of ARPEFS,[6] the expression for $\chi(k)$ can be written as

$$\chi(k)=2\sum_j \frac{\cos\beta_j}{\cos\gamma}\frac{|f(\theta_j)|}{R_j}e^{-\Delta R_j/\lambda}e^{-\sigma_j^2(1-\cos\theta_j)k^2} \times\cos[kR_j(1-\cos\theta_j)+\phi_j] . \tag{4}$$

The summation is over all atoms near the adsorbed "source" atom from which core-level photoemission originates. Here, β_j is the angle between the photon polarization vector and the vector connecting the emitting atom and the jth scattering atom, R_j is the distance from the photoemitter to the jth scattering atom, and γ is the angle between the emission direction and the photon polarization vector. The k-dependent complex scattering factor $f(\theta_j)$ for a given scattering angle θ_j can be divided into the magnitude $|f(\theta_j)|$ and the phase ϕ_j. The emission-angle-dependent path-length difference is given by $\Delta R_j=R_j(1-\cos\theta_j)$. The temperature effect is introduced as a Debye-Waller factor, where σ_j is the mean-square relative displacement (MSRD) between the photoemitter and the jth scattering atom, projected on the photoelectron momentum change direction. Inelastic losses due to excitation of plasmons and electron-hole pairs by the energetic photoelectron are incorporated in an electron mean free path λ.

The cosinusoidal dependence of the $\chi(k)$ function permits a Fourier transformation, yielding an amplitude spectrum peaked near various scattering path-length differences. Fourier spectra for the [111] and [110] data at the two temperatures are given in Fig. 3. A V_0 value of 10 eV was used. Forward ($\theta_j=0°$) and backward ($\theta_j=180°$) scatterings give the strongest signals: the strong feature at a path-length difference $\sim$4.6 Å in the [110] direction arises from a nearest-neighbor Ni atom located directly behind Cl along the [110] direction, at a Cl—Ni bond length of $\sim$2.3 Å. Atop and bridge adsorption sites are excluded because they have no backscatter-

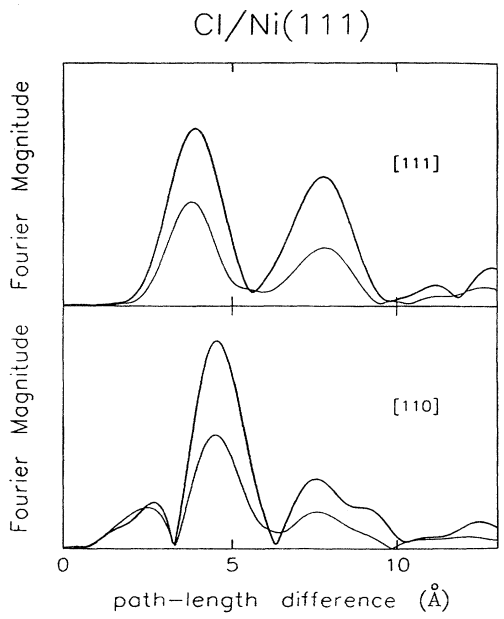

FIG. 3. Fourier spectra for the [111] and the [110] geometries at two temperatures, 120 and 300 K. The heavier curves are the spectra at 120 K.

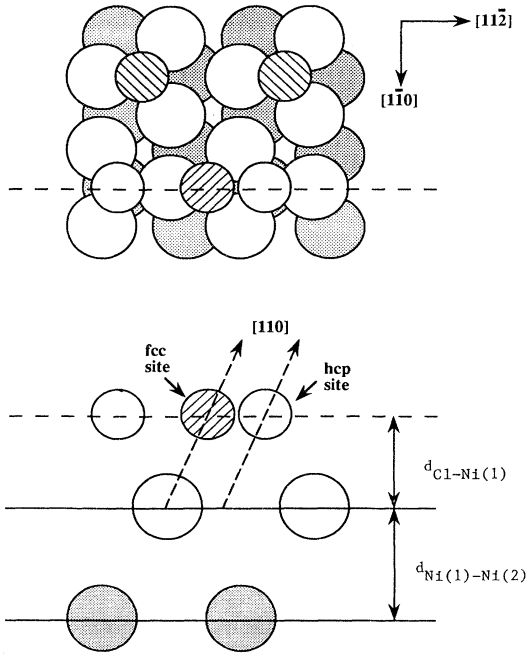

FIG. 4. Top and side views of the $\sqrt{3}\times\sqrt{3}R30°$ Cl/Ni(111) structure. The smaller shaded circles represent the Cl atoms in the fcc sites, while the smaller open circles represent the Cl atoms in the hcp sites. The side view (lower panel) corresponds to a cut in the plane shown the dashed line in the top view (upper panel).

ing atom along the [110] direction to give the strong peak at ~4.6 Å. However, there are two different threefold hollow adsorption sites, which are called the fcc and hcp sites, respectively. The fcc sites are directly above atoms in the third substrate layer, while the hcp sites are directly above atoms in the second substrate layer. Figure 4 illustrates that one of the nearest-neighbor Ni atom lies behind the Cl atom along the [110] direction in the fcc site, but not in the hcp site. Therefore, the strong Fourier backscattering peak in the [110] direction indicates that the fcc threefold hollow site is the one occupied in the $\sqrt{3}\times\sqrt{3}R30°$ Cl/Ni(111) system. Furthermore, the two peaks at ~7.6 and ~9.1 Å in the [110] direction can be attributed mainly to scattering from the atoms in the second Ni(110) plane, while the first peak at ~2.5 Å in the [110] direction corresponds to scattering from two nearest-neighboring atoms symmetrically located at either side of the plane containing the [111] and [110] directions.

Fourier spectra in the [111] direction show two peaks at ~3.9 and ~7.8 Å. The first peak is due to scattering from the three nearest-neighboring atoms in the first Ni layer, while the second peak corresponds to scattering from the three third-nearest-neighbor atoms in the second Ni layer. Thus, the normal-emission data suggest that we can determine the distance of Cl to both the first and second Ni layers, providing information about the substrate surface relaxation.

B. Multiple-scattering analysis

ARPEFS studies[1–5] have shown that the detailed quantitative geometric structures can be obtained by comparing experimental $\chi(k)$ curves with theoretical calculations based on MSSW theory,[7] which comprehensively describes the ARPEFS scattering process. The MSSW calculation requires as input both structural and nonstructural parameters. The nickel and chlorine phase shifts were available from previous calculations.[5,17,18] The mean free path was included in an exponential factor, $e^{-r/\lambda}$, with $\lambda=ck$ and $c=0.75$. Thermal effects were treated using a correlated Debye model which included surface-layer-dependent and anisotropic MSRD's.[7] The nickel bulk Debye temperature was taken as 390 K, while the nickel surface Debye temperature was set to 276 K, which assumes that the surface nickel atoms have a MSRD twice as that of the bulk. The Debye temperature for the Cl overlayer was estimated to be 355 K from the nickel surface Debye temperature adjusted for the difference in masses. Surface Debye temperatures for both Cl and Ni were, however, varied in the calculations based on the above-estimated values. In addition, the emission and polarization angles (±3°), the experimental temperature (120±10 K), and the inner potential (10±5 eV) were allowed to vary in the calculations.

First, both the [111] and the [110] experimental $\chi(k)$ curves at the two temperatures were smoothed by Fourier filtering out the high-frequency portion of the data (path-length differences larger than 10.0 Å). Thus, the cutoff at about 10.0 Å eliminates high-frequency noise and retains all the real signals from down to the second substrate layer. Also, the cutoffs below 1.8–2.0 Å were

made due to uncertainties of the low-frequency portion of the data. All subsequent comparisons of theory with experiment were done with the filtered data, 2.0–10.0 Å for the [111] data and 1.8–10.0 Å for the [110] data. The MSSW calculations were performed with the same path-length difference cutoffs.

The fcc threefold adsorption site had already been determined for the $\sqrt{3}\times\sqrt{3}R30°$ Cl/Ni(111) system from the Fourier analysis above. Comparisons of the MSSW calculations with the experimental data confirm this result. The $\chi(k)$ curves for two different threefold adsorption geometries (fcc and hcp) were calculated using the bulk Ni spacing (2.03 Å) with a Cl—Ni bond length of 2.3 Å estimated from the Fourier analysis. Figure 5 shows the comparison of the calculated $\chi(k)$ curves with the experimental data for the [111] and [110] directions at 120 K, respectively. By visual inspection, the calculated curve in the [110] direction for the fcc site unambiguously resembles the experimental data more than that for the hcp site, while in the [111] direction, it is not clear which calculated $\chi(k)$ more closely resembles the experimental data. Since there is a backscattering atom near the photoemitter for the fcc site, but not for the hcp site in the [110] direction, the calculated $\chi(k)$ curve for the hcp site has rather different features and weaker amplitude as compared with that for the fcc site. Thus, MSSW calculations provide strong evidence to support the fcc threefold site, consistent with the Fourier analysis. However, there are still large differences between the experimental $\chi(k)$ curve and the calculations for the fcc site using nonoptimized geometrical parameters. This suggests possible substrate surface relaxation in the $\sqrt{3}\times\sqrt{3}R30°$ Cl/Ni(111) system.

To derive a detailed quantitative structure, we optimized both structural and nonstructural parameters to achieve the best agreement between the theory and the experiment. An R factor (reliability factor) was used as a quantitative measure of the fit between the experiment and the theory. The optimum geometrical parameters were obtained when a minimal R factor defined by

$$R=\frac{\int[\chi_E(k)-\chi_T(k)]^2dk}{\int[\chi_T(k)]^2dk}, \tag{5}$$

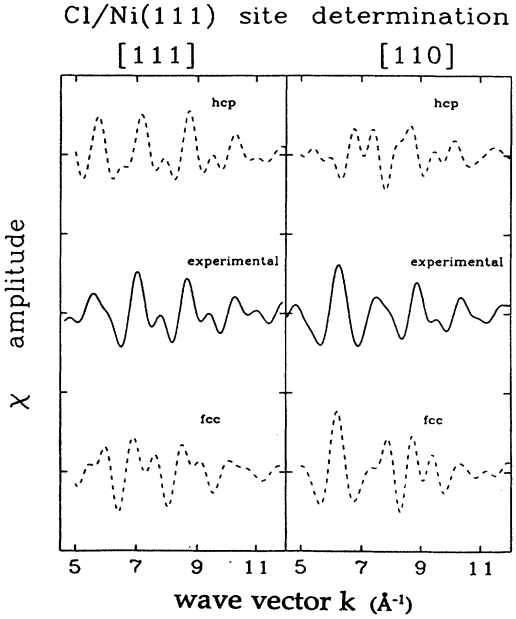

FIG. 5. Adsorption site determination for the [111] and the [110] geometries at 120 K. The experimental curves (solid lines) are compared to the MSSW calculated curves (dashed lines) for two kinds of unreconstructed threefold hollow adsorption geometries (fcc and hcp).

was reached. Here, E and T denote experiment and theory. The R factors were calculated over the k range 5.2–11.2 Å^{-1}.

In recent ARPEFS studies,[5,8] an automatic routine was successfully used to search many parameters simultaneously with a reasonable number of iterations. The detailed procedure of this routine has been described previously. No lateral substrate relaxation and no corrugation of the second substrate layer were considered because of the $\sqrt{3}\times\sqrt{3}R30°$ structure of the Cl/Ni(111) system. The experimental data were fitted with two structural parameters $d_{\text{Cl-Ni(1)}}$, the vertical distance of Cl to the first Ni layer, and $d_{\text{Cl-Ni(2)}}$, the vertical distance of Cl to the

TABLE I. Summary of the structural results (in Å) determined from MSSW analysis. The statistical errors associated with each parameter for the four data sets are given in parentheses (Ref. 5). The structural parameter values in the upper panel are derived directly from fits of the data, while those in the lower panel were derived by subtracting two corresponding values above the line.

Parameter	$[111]_{120\text{ K}}$	$[111]_{300\text{ K}}$	$[110]_{120\text{ K}}$	$[110]_{300\text{ K}}$	Avg[a] (stat)	Avg[b] (scat)	This work[c]
$d_{\text{Cl-Ni(1)}}$	1.831(8)	1.828(10)	1.848(9)	1.844(16)	1.837(5)	1.838(8)	1.837(8)
$d_{\text{Cl-Ni(2)}}$	3.767(10)	3.763(13)	3.754(14)	3.761(40)	3.763(7)	3.761(5)	3.763(7)
Cl—Ni (bond length)					2.332(4)	2.333(6)	2.332(6)
$d_{\text{Ni(1)-Ni(2)}}$					1.926(10)	1.923(9)	1.926(11)

[a]Statistical errors only: Standard deviation.

[b]Standard deviation from the scatter of results.

[c]Final adopted values, with standard deviation taken as the higher of a and b above. Not included in these values and error estimate are any possible offset due to (unknown) systematic error.

second Ni layer, while other nonstructural parameters such as electron emission angles, adsorbate and substrate surface Debye temperatures, the experimental temperature, and the inner potential were treated as adjustable parameters with reasonable initial guesses and bounds. The emission angles were found to be $<3°$ from the expected values for all the data sets. The inner potential for the optimum geometry was 10 ± 2 eV, and the experimental temperature was optimized to be 120 ± 5 K. R-factor minima lay in the small range $R=0.05-0.13$ in the various calculations.

The structural parameters determined from the best fits are listed in Table I, with statistical errors in parentheses. The error associated with each parameter was estimated as described in our previous study.[5] The best fits of the MSSW calculations to the filtered (10.0 Å) experimental $\chi(k)$ curves are shown in Figs. 6 and 7 for the [111] and [110] geometries at the two temperatures, respectively. Agreements between the theoretical and experimental curves are excellent. From Table I, we can see that the structural parameters obtained from the four data sets were consistent, especially for the data at different temperatures with a given geometry. There are larger errors for the $d_{\text{Cl-Ni(2)}}$ parameter in the [110] direction than those in the [111] direction, showing different sensitivity of a given data set to each structural parameter due to the directional sensitivity of ARPEFS.

Figure 8 shows R-factor plots for the [111] and [110] geometries at the two temperatures, calculated by varying the $d_{\text{Cl-Ni(1)}}$ and $d_{\text{Cl-Ni(2)}}$ distances, respectively, while other parameters were fixed in their optimum values. The R-factor curvature for the $d_{\text{Cl-Ni(2)}}$ distance in the [111] direction is steeper than that in the [110] direction, giving smaller error bars for the $d_{\text{Cl-Ni(2)}}$ distance in the [111] geometry. Moreover, the R-factor minima were smaller for a given geometry at the lower temperature, due to the increased signal-to-noise ratio. The interlayer spacing between the first and the second Ni layers can thus be determined more accurately from the analysis of

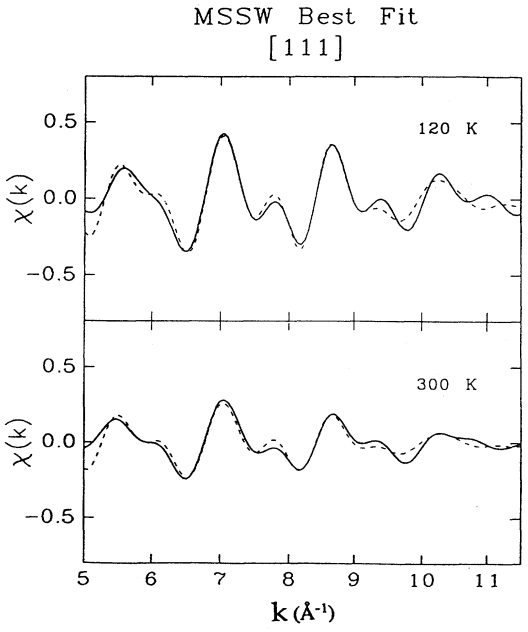

FIG. 6. The best fits of the MSSW calculations (dashed curves) to the filtered (10.0 Å) ARPEFS data (solid curves) for the [111] geometry at two temperatures, 120 and 300 K.

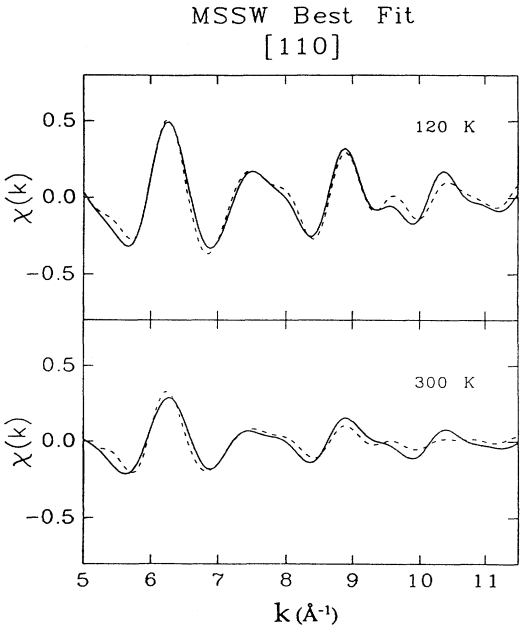

FIG. 7. The best fits of the MSSW calculations (dashed curves) to the filtered (10.0 Å) ARPEFS data (solid curves) for the [110] geometry at two temperatures, 120 and 300 K.

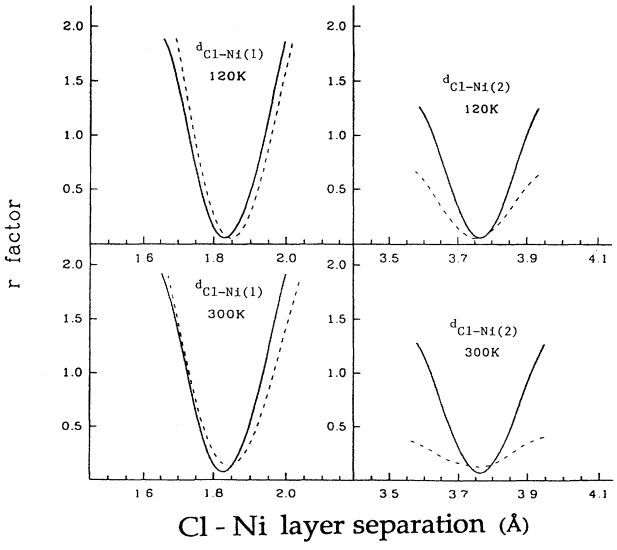

FIG. 8. R-factor plots for the [111] and the [110] geometries at two temperatures, 120 and 300 K, calculated by varying the $d_{\text{Cl-Ni(1)}}$ and the $d_{\text{Cl-Ni(2)}}$ distances, respectively, while other parameters were fixed in their optimum values.

the low-temperature [111] data.

The top and side views of the $\sqrt{3}\times\sqrt{3}R30°$ Cl/Ni(111) structure are shown in Fig. 4. From Table I, the $d_{\text{Cl-Ni(1)}}$ distance of 1.837(8) Å gives a Cl—Ni bond length of 2.332(6) Å. The $d_{\text{Cl-Ni(2)}}$ distance of 3.763(7) Å then yields interlayer spacing between the first and the second Ni layers $d_{\text{Cl-Ni(2)}}$ of 1.926(11) Å, showing an approximate 5% contraction from the bulk value of 2.03 Å.

IV. DISCUSSION

The vertical distance of Cl to the first Ni layer $d_{\text{Cl-Ni(1)}}$ of 1.837(8) Å obtained from this study is 0.08 Å smaller than the recent SEXAFS study[13] by Kuroda *et al.* This difference is beyond the standard error of each of the two techniques. However, studies on the $p(2\times2)$ S/Ni(111) system using several different techniques also showed rather different results for the vertical distance of S to the first Ni layer $d_{\text{S-Ni(1)}}$, ranging from 1.40 to 1.66 Å.[14,19–22] For example, a SEXAFS study[14] by the same group gave the $d_{\text{S-Ni(1)}}$ distance at 1.66 Å, while a LEED study[19] by Mitchell *et al.* showed a distance of 1.50 Å, a 0.16-Å difference. Furthermore, a recent low-temperature ARPEFS study[8] on the same system found the S-Ni(1) distance of 1.54 Å, which is closer to the LEED study. We can see that the distances of adsorbate to the first substrate layer from SEXAFS studies on both $p(2\times2)$ S/Ni(111) and $\sqrt{3}\times\sqrt{3}R30°$ Cl/Ni(111) systems tend to be larger than the results obtained from LEED and ARPEFS studies. This suggests some sort of unknown systematic errors among these techniques. With recent improvements in the quality of data and analysis, it now appears that ARPEFS, LEED, and SEXAFS may be inherently capable of yielding structural parameters of high precision: $\pm0.01-0.02$ Å in the case of ARPEFS, for example. If the remaining discrepancies among the three methods arise from systematic errors, the resolution of those errors is important.

The current ARPEFS study found a 0.104-Å for 5% contraction of the topmost Ni interlayer spacing as compared with that of the bulk for the $\sqrt{3}\times\sqrt{3}R30°$ Cl/Ni(111) system by analyzing structural information from the first and the second Ni layers. However, Kuroda *et al.* reported no relaxation in the same Cl/Ni(111) system, in contrast to a significant contraction of 15% in the $p(2\times2)$ S/Ni(111) system using their SEXAFS results combined with those from the x-ray standing-wave method. Figure 9 shows the comparisons of the experimental data for both the [111] and the [110] geometries at 120 K with the calculated $\chi(k)$ curves based on the bulk Ni spacing (2.03 Å), while other parameters were kept fixed at their optimum values. By visual inspection, the agreements for both geometries are very poor, indicating that the substrate surface relaxation is required to obtain the fits between the experiment and the theory shown in Figs. 6 and 7. Although a combination of x-ray standing-wave and SEXAFS studies provides direct information about the relaxation of the first substrate layer relative to the bulk position, the information about the topmost interlayer spacing is indirect, as it requires the second substrate layer to remain in the bulk position.

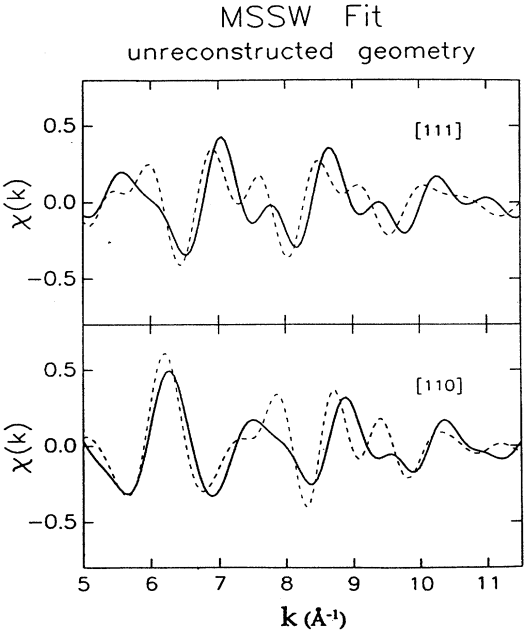

FIG. 9. Comparisons of the filtered (10.0 Å) ARPEFS data (solid curves) to the MSSW calculations (dashed curves) for the [111] and [110] geometries at 120 K. The MSSW curves are calculated with the bulk Ni spacing (2.03 Å), while all the other parameters are kept fixed at their optimum values.

Low-temperature ARPEFS itself, however, can obtain the topmost interlayer spacing directly for the $\sqrt{3}\times\sqrt{3}R30°$ Cl/Ni(111) system, due to its ability to probe the second substrate layer.

Studies on the clean Cu(111) surface[23] showed a $(0.7\pm0.5)\%$ *contraction* of the topmost interlayer spacing, smaller than the contractions on more open (001) and (110) surfaces. If the clean Ni(111) surface also has little contraction in the topmost interlayer spacing, a 5% contraction in the $\sqrt{3}\times\sqrt{3}R30°$ Cl/Ni(111) system is much larger than that of the clean Ni(111) surface, indicating the adsorbate-induced contraction. In contrast to the Cl/Ni(111) system, studies of adsorbates on fcc (001) surfaces such as S- and Cl-covered Ni(001) and Cu(001) have shown *expansions* of the topmost interlayer spacing,[1,5,8–11,24,25] which has been attributed to metal-metal bond weakening induced by adsorption. The mechanism for contraction is not clear in the $\sqrt{3}\times\sqrt{3}R30°$ Cl/Ni(111) system.

The previous low-temperature ARPEFS study on the Cl/Cu(001) system showed that cooling the lattice effectively extends the range of ARPEFS to the fourth substrate layer.[5] However, in this study, we could only obtain the distances from Cl to the first and to the second layers. In Fig. 2, we note consistent high-frequency oscillations in the experimental $\chi(k)$ curves at two temperatures, as compared with the filtered (10-Å) curves shown in Figs. 6 and 7, suggesting the existence of real signals at large path-length differences (>10 Å). Figure 10 shows the experimental Fourier spectrum in the [111] direction

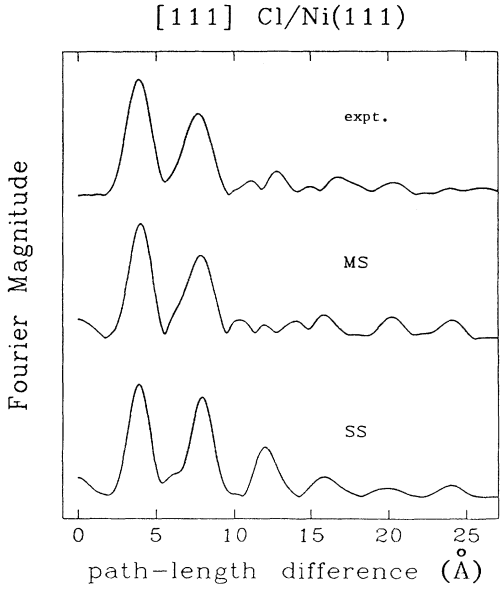

FIG. 10. Comparison among the Fourier spectra for the [111] geometry at 120 K: experimental Fourier spectrum with those spectra obtained from single- and multiple-scattering calculations based on the optimized parameters.

at 120 K, with the Fourier spectra obtained from single- and multiple-scattering calculations based on the optimized parameters. The agreement among these three Fourier transform spectra in the range 10–25 Å is not good enough to permit a quantitative structural interpretation, but it is intriguing. The single-scattering curve shows peaks spaced at 4-Å intervals, consistent with backscattering from the Ni(111) planes spaced at 2.03 Å. In fact, weak peaks near 20 and 24 Å, consistent with scattering from the fifth and sixth layers, appear in all three curves. However, for intermediate path-length differences 10–18 Å, single scattering yields only two peaks, while both multiple scattering and experiment show four. The latter two curves agree only in regard to the overall intensity of the pattern of four peaks, but not with respect to their exact positions or detailed intensity pattern. We therefore conclude that the single-scattering calculation omits important (multiple-scattering) effects which show up in the experimental curve, and the multiple-scattering theory, as we have applied it, does not model these effects accurately.

V. CONCLUSION

We have presented a low-temperature ARPEFS study of the $\sqrt{3}\times\sqrt{3}R30°$ Cl/Ni(111) system. The surface was determined by two methods: Fourier analysis, which gives qualitative structural information, and the multiple-scattering spherical-wave (MSSW) analysis, which yields more quantitative results. This ARPEFS study provided a clear distinction between the two inequivalent threefold hollow sites using directional sensitivity of ARPEFS and found that the fcc threefold hollow site is favored for the $\sqrt{3}\times\sqrt{3}R30°$ Cl/Ni(111) system. Low-temperature ARPEFS allows us to determine structural parameters more accurately due to the increased signal-to-noise ratio. MSSW analysis found the Cl atom adsorbed in the fcc threefold hollow site, 1.837(8) Å above the first nickel layer with a Cl—Ni bond length of 2.332(6) Å and an approximate 5% contraction between the first and the second nickel layers, in disagreement with a recent study[13] by Kuroda *et al.*

ACKNOWLEDGMENTS

This was supported by the Director, Office of Energy Research, Office of Basic Energy Sciences, Division of the U.S. Department of Energy under Contract No. DE-AC03-76SF00098. The experiments were performed at the National Synchrotron Light Source at Brookhaven National Laboratory, which is supported by the U.S. Department of Energy's Office of Basic Energy Sciences. We are greatly indebted to J. Stohr for the loan of the Ni(111) single crystal and to B. Karlin for providing assistance in running the monochromator. Z.H. wishes to acknowledge King Fahd University of Petroleum and Minerals for the grant of a sabbatical leave.

*Present address: Department of Chemistry, Nevada University, Las Vegas, NV 98154.

[1]J. J. Barton, C. C. Bahr, S. W. Robey, Z. Hussain, E. Umbach, and D. A. Shirley, Phys. Rev. B **34**, 3807 (1986).

[2]S. W. Robey, J. J. Barton, C. C. Bahr, G. Liu, and D. A. Shirley, Phys. Rev. B **35**, 1108 (1987).

[3]L. J. Terminello, X. S. Zhang, Z. Q. Huang, S. Kim, A. E. Schach von Wittenau, K. T. Leung, and D. A. Shirley, Phys. Rev. B **38**, 3879 (1988).

[4]X. S. Zhang, L. J. Terminello, S. Kim, Z. Q. Huang, A. E. Schach von Wittenau, and D. A. Shirley, J. Chem. Phys. **89**, 6538 (1988).

[5]L. Q. Wang, A. E. Schach von Wittenau, Z. G. Ji, L. S. Wang, Z. Q. Huang, and D. A. Shirley, Phys. Rev. B **44**, 1292 (1991).

[6]J. J. Barton, C. C. Bahr, Z. Hussain, S. W. Robey, J. G. Tobin, L. E. Klebanoff, and D. A. Shirley, Phys. Rev. Lett. **51**, 272 (1983).

[7]J. J. Barton, S. W. Robey, and D. A. Shirley, Phys. Rev. B **34**, 778 (1986).

[8]A. E. Schach von Wittenau, L. Q. Wang, Z. G. Ji, Z. Q. Huang, T. Shulman, and D. A. Shirley (unpublished).

[9]F. Jona, D. Westphal, A. Goldmann, and P. M. Marcus, J. Phys. C **16**, 3001 (1983).

[10]P. H. Citrin, D. R. Hamann, L. F. Mattheiss, and J. E. Rowe, Phys. Rev. Lett. **49**, 1712 (1982).

[11]J. R. Patel, D. W. Berreman, F. Sette, P. H. Citrin, and J. E. Rowe, Phys. Rev. B **40**, 1330 (1989).

[12]M. D. Crapper, C. E. Riley, P. J. J. Sweeney, C. F. McConville, D. P. Woodruff, and R. G. Jones, Surf. Sci. **182**, 213 (1987).

[13]M. Funabashi, Y. Kitajima, T. Yokoyama, T. Ohta, and H. Kuroda, Physica B **158**, 664 (1989).
[14]T. Yokoyama, M. Funabashi, Y. Kitajima, T. Ohta, and H. Kuroda, Physica B **158**, 643 (1989).
[15]P. L. Cowan, S. Brennan, R. D. Deslattes, A. Henins, T. Jach, and E. G. Kessler, Nucl. Instrum. Methods A **246**, 154 (1986).
[16]S. D. Kevan, Ph.D. thesis, University of California, Berkeley, 1980 (unpublished).
[17]P. J. Orders and C. S. Fadley, Phys. Rev. B **27**, 781 (1983).
[18]J. B. Pendry, *Low Energy Electron Diffraction* (Academic, London, 1974).
[19]Y. K. Wu and K. A. R. Mitchell, Can J. Chem. **67**, 1975 (1989).
[20]T. Fauster, H. Durr, and D. Hartwig, Surf. Sci. **178**, 657 (1986).
[21]D. R. Warburton, P. L. Wincott, G. Thornton, F. M. Quinn, and D. Norman, Surf. Sci. **211/212**, 71 (1989).
[22]J. E. Demuth, D. W. Jepsen, and P. M. Marcus, Phys. Rev. Lett. **32**, 1182 (1974).
[23]S. A. Lindgren, L. Wallden, J. Rundgren, and P. Westrin, Phys. Rev. B **29**, 576 (1984).
[24]J. E. Demuth, D. W. Jepsen, and P. M. Marcus, Phys. Rev. Lett. **31**, 540 (1973); **32**, 1184 (1974).
[25]T. Yokoyama, Y. Takata, T. Ohta, M. Funabashi, Y. Kitajima, and H. Kuroda, Phys. Rev. B **42**, 7000 (1990).